Tight focusing of laser beams in a λ/2-microcavity

Dmitry Khoptyar, Raphael Gutbrod, Anna Chizhik, Jörg Enderlein, Frank Schleifenbaum, Mathias Steiner, Alfred J. Meixner*

Institute of Physical and Theoretical Chemistry, Tuebingen University, Auf der Morgenstelle 8, 72076 Tuebingen, Germany
Correspondent author: alfred.meixner@uni-tuebingen.de
http://www.uni-tuebingen.de/Meixner/index.html

Abstract: We evaluate the field distribution in the focal spot of the fundamental Gaussian beam as well as radially and azimuthally polarized doughnut beams focused inside a planar metallic sub-wavelength microcavity using a high numerical aperture objective lens. We show that focusing in the cavity results in a much tighter focal spot in longitudinal direction compared to free space and in spatial discrimination between longitudinal and in-plane field components. In order to verify the modeling results we experimentally monitor excitation patterns of fluorescence beads inside the λ/2-cavity and find them in full agreement to the modeling predictions. We discuss the implications of the results for cavity assisted single molecular spectroscopy and intra-cavity single molecular imaging.

© 2008 Optical Society of America

OCIS codes: (180.1790) Confocal microscopy; (180.2520) Fluorescence microscopy; (110.0180) Microscopy; (260.1960) Diffraction theory.

References and links

1. W. E. Moerner "A Dozen Years of Single-Molecule Spectroscopy in Physics, Chemistry, and Biophysics," J. Phys. Chem. B **106**, 910-927 (2002).
2. W. E. Moerner and David P. Fromm, "Methods of single-molecule fluorescence spectroscopy and microscopy," Rev. Sci. Instrum. **74**, 3597-3619 (2003).
3. F. Kulzer and M. Orrit, "Single-Molecule Optics," Ann. Rev. Phys. Chem. **55**, 585-611 (2004).
4. L. Novotny, M. R. Beversluis, K. S. Youngworth, and T. G. Brown, "Longitudinal Field Modes Probed by Single Molecules," Phys. Rev. Lett. **86**, 5251-5254 (2001).
5. H. Piwonski, C. Stupperich, A. Hartschuh, J. Sepiol, A. Meixner, and J. Waluk, "Imaging of tautomerism in a single molecule," J. Am. Chem. Soc. **127**, 5302-5303 (2005).
6. A. V. Failla, H. Qian, H. Qian, A. Hartschuh, and A. J. Meixner, "Orientational imaging of subwavelength Au particles with higher order laser modes," Nano. Lett. **6**, 1374 -1378 (2006).
7. M. Steiner, F. Schleifenbaum, C. Stupperich, A. V. Failla, A.Hartschuh , and A. J. Meixner, "Microcavity-Controlled Single-Molecule Fluorescence," ChemPhysChem **6**, 2190-2196 (2005).
8. M. Steiner, F. Schleifenbaum, C. Stupperich, A.V. Failla, A. Hartschuh, and A. J. Meixner, "A new microcavity design for single molecule detection," J. Lumin. **119–120,** 167–172 (2006).
9. M. Steiner, A. Hartschuh, R. Korlacki, and A. J. Meixner, "Highly efficient, tunable single photon source based on single molecules," Appl. Phys. Lett. **90,** 183122-1-3 (2007).
10. M. Steiner, H Qian, A. Hartschuh, and A. J. Meixner, "Controlling nonequilibrium phonon populations in single-walled carbon nanotubes," Nano. Lett. **7**, 2239-2242 (2007).
11. P. Andrew and W. L. Barnes, "Forster energy transfer in an optical microcavity," Science **290**, 785-788 (2000).
12. M. Hopmeier, W. Guss, M. Deussen, E. O. Göbel, and R. F. Mahrt, "Enhanced dipole-dipole interaction in a polymer microcavity," Phys Rev. Lett. **82**, 4118- 4121 (1999).
13. D. P. Biss and T. G. Brown, "Cylindrical vector beam focusing through a dielectric interface," Opt. Express **9**, 490-497 (2001).
14. A.S. van de Nes, P. R. T. Munro, S. F. Pereira, J. J. M. Braat, and P. Török, "Cylindrical vector beam focusing through a dielectric interface: comment," Opt. Express **12,** 967-969 (2003).

15. A. S. van de Nes, L. Billy, S. F. Pereira, and J. J. M. Braat, "Calculation of the vectorial field distribution in a stratified focal region of a high numerical aperture imaging system," Opt. Express **12**, 1281-1293 (2004).
16. H. Rigneault, S. Monneret, and C. I. Westbrook, "Resonant focusing in a planar microcavity," J. Opt. Soc. Am. B **15**, 2712-2715 (1998).
17. B. Richards and E. Wolf, "Electromagnetic diffraction in optical systems II. Structure of the image field in an aplanatic system," Proc. R. Soc. London, Ser. **A 253**, 358-379 (1959).
18. L. Novotny and B. Hecht , *Principles of Nanooptics* (Cambridge University Press 2006).
19. M. Born and E. Wolf, *Principles of optics* (Cambridge University Press 1999).
20. N. Bokor, Y. Iketaki, T. Watanabe, and M. Fujii, "Investigation of polarization effects for highnumerical-aperture first-order Laguerre-Gaussian beams by 2D scanning with a single fluorescent microbead," Opt. Express **13,** 10440-10447 (2005).
21. J. Enderlein, "Theoretical study of detection of a dipole emitter through an objective with high numerical aperture," Opt. Lett. **25,** 634-636 (2000).
22. A. V. Failla, S. Jäger, T. Züchner, M. Steiner, and A. J.Meixner, "Topology measurements of metal nanoparticles with 1 nm accuracy by Confocal Interference Scattering Microscopy," Opt. Express **15,** 8532-8542 (2007).

1. Introduction

Single molecular (SM) spectroscopy and imaging applied to fundamental material-related studies as well as to nano/bio photonics applications are the current topic of active research [1-3]. In particular, SM spectroscopy with azimuthally and radially polarized doughnut beams [4-6] is a new powerful technique that enables precise determination of SM transition dipole moment orientation providing deeper inside into SM photo-physics and structural properties of the host materials and adsorbing interfaces.

Another recently emerging technique with great potential for the novel nano-scale sensors and single emitter photon sources is sub-wavelength cavity assisted SM spectroscopy [7-10]. There, due to the modification of the density of the optical states inside the planar sub-wavelength cavity the emission properties of SM can be strongly modified, which includes spectral and spatial (angular) redistribution of the spontaneous emission as well as enhancement and inhibition of the spontaneous emission rate. This enables tailoring of the SM emission properties to meet the nano-photonics application needs and, notably, opens novel functionalities as e.g. Förster energy transfer control [11],[12].

An optimal microcavity design requires in depth understanding of the cavity electrodynamics; in particular excitation field distribution that arises in the cavity after tight focusing of the excitation beam. While tight focusing of laser beams on the dielectric interfaces and in multilayer dielectric structures has being discussed [13-15] rigorous treatment of the focusing inside metallic sub-wavelength cavity is still lacking [16].

In the first section of the paper we develop a model for evaluation of the electromagnetic field distribution resulting form the tight focusing of the fundamental Hermit-Gaussian (HGB) as well as radially (RPDB) and azimuthally (APDB) polarized doughnut beams inside a sub-wavelength microcavity composed of two metallic mirrors.

In the second section we review computation results and discuss cavity electrodynamics effects essential for optimum microcavity design as well as consistent interpretation of SM imaging and spectroscopic experiments.

In the third section we present and discuss excitation patterns of fluorescence beads inside the sub-wavelength microcavity obtained using APDB and RPDB that provide clear and conclusive experimental confirmation of the present modeling.

2. Model

According to Richards and Wolf's [17] model for tight focusing of laser beams recently reviewed in [18] an electromagnetic field distribution arising from focusing of the fundamental x-polarized HGB by an aplanatic lens is given by the following expression:

$$E_{HG} = E_0 \frac{ikfe^{-ikf}}{2} \left(\begin{bmatrix} L_{0,0,0}(\rho,z) + L_{2,0,0}(\rho,z)\cos(2\varphi) \\ L_{2,0,0}(\rho,z)\sin(2\varphi) \\ 0 \end{bmatrix} + \begin{bmatrix} L_{0,1,0}(\rho,z) - L_{2,1,0}(\rho,z)\cos(2\varphi) \\ -L_{2,1,0}(\rho,z)\sin(2\varphi) \\ -2iL_{1,0,1}(\rho,z)\cos(\varphi) \end{bmatrix} \right). \quad (1)$$

There (ρ, z, φ) are the cylindrical coordinates with $z = 0$ correspondent to the principal focal point of the lens with focal length f, $k = 2\pi/\lambda$ is a wave-vector of the field with the wavelength λ, and E_0 denotes the field amplitude. First and second vector columns in (1) correspond to E_x, E_y, and E_z field components of the s and p waves, respectively. The function $L_{n,m,l}(\rho, z)$ is defined as follows:

$$L_{n,m,l}(\rho, z) = \int_0^{\theta_{MAX}} f_w(\theta) J_n(kn_r\rho\sin(\theta))\exp(ik_z n_r z)\cos(\theta)^{m+1/2}\sin(\theta)^{l+1} d\theta . \quad (2)$$

There, $k_z = k\cos(\theta)$, n_r is the medium refractive index, $J_n(x)$ is the n-th order Bessel function, and $f_w(\theta)$ is given by:

$$f_w(\theta) = \exp\left(-\frac{1}{f_0^2} \frac{\sin(\theta)^2}{\sin(\theta_{max})^2} \right). \quad (3)$$

In (3) the filling factor f_0 is defined as $f_0 = w_0 f^{-1}\sin(\theta_{max})^{-1}$; that gives a ratio of the beam waist (w_0) to the lens aperture radius $f\sin(\theta_{max})$. Finally θ_{max} is the maximum acceptance angle of the objective lens.

Using the same notation for RPDB, that is essentially a pure p-wave given by the superposition of x-polarized Hermit-Gaussian (1,0) and y-polarized Hermit-Gaussian (0,1) beams, we have:

$$E_{RPDB} = E_0 \frac{if^2 k \exp(-ikf)}{2w_0} \begin{pmatrix} 4iL_{1,1,1}(\rho,z)\cos(\varphi) \\ 4i L_{1,1,1}(\rho,z)\sin(\varphi) \\ -4L_{0,0,2}(\rho,z) \end{pmatrix}. \quad (4)$$

Similarly, for the focusing of APDB, that is a pure s-wave given by the superposition of y-polarized Hermit-Gaussian (1,0) and x-polarized Hermit-Gaussian (0,1) beams, the modeling results in:

$$E_{APDB} = E_0 \frac{if^2 k \exp(-ikf)}{2w_0} \begin{pmatrix} 4iL_{1,0,1}(\rho,z)\sin(\varphi) \\ -4iL_{1,0,1}(\rho,z)\cos(\varphi) \\ 0 \end{pmatrix}. \quad (5)$$

Formulas (1), (4), and, (5) using (2), and (3), establish the focal field distribution for a beam refracted by an aplanatic lens in free space [18].

When the beam is focused inside a sub-wavelength cavity the intra-cavity field distribution is a result of interference of the far-field beam components impinging on the cavity at different angles and experiencing multiple reflections between the cavity mirrors. By tracing angle-dependent beam components inside the cavity and taking into account the

difference in the Fresnel coefficient for metallic mirrors correspondent to s-and p-polarizations we arrive at the following model for tight beam focusing inside the microcavity. In the framework of the current notation formulas (1), (4), and (5) are still hold, provided $L_{n,m,l}(\rho,z)$ is redefined as follows:

$$L_{n,m,l}^{\alpha,\beta}(\rho,z) = \int_0^{\theta_{MAX}} f_w(\theta) J_n\left(kn_r\rho\sin(\theta)\right) f_\beta^\alpha(z,\theta,L_c)\cos(\theta)^{m+1/2}\sin(\theta)^{l+1}d\theta . \quad (6)$$

There the intra-cavity transmission coefficient $f_\beta^\alpha(z,\theta,L_c)$ replacing the free space phase propagation factor $\exp(ik_z z)$ in (2) determines the intra-cavity distribution of the longitudinal (E_z) and in-plane (E_x, E_y) field components ($\beta = z$ or x, y, respectively) that result from the plane s- or p- polarized ($\alpha = s$ or p, respectively) wave impinging on the cavity with thickness L_c at an angle θ. After designating the intra-cavity refractive index as n_{ic}, $f_\beta^\alpha(z,\theta,L_{cav})$ takes the form:

$$f_{x,y}^s(z,\theta,L_c) = t_1^s(\theta)\frac{\exp(ik_z n_{ic} z) + r_2^s(\theta)\exp[ik_z n_{ic}(L-z)]}{1 - r_1^s(\theta)r_2^s(\theta)\exp(2ik_z n_{ic} L)} , \quad (7)$$

$$f_z^s(z,\theta,L_c) = 0 , \quad (8)$$

$$f_{x,y}^p(z,\theta,L_c) = t_1^p(\theta)\frac{\exp(ik_z n_{ic} z) - r_2^p(\theta)\exp[ik_z n_{ic}(L-z)]}{1 - r_1^p(\theta)r_2^p(\theta)\exp(2ik_z n_{ic} L)} , \quad (9)$$

$$f_z^p(z,\theta,L_c) = t_1^p(\theta)\frac{\exp(ik_z n_{ic} z) + r_2^p(\theta)\exp[ik_z n_{ic}(L-z)]}{1 - r_1^p(\theta)r_2^p(\theta)\exp(2ik_z n_{ic} L)} . \quad (10)$$

There $t_i^\alpha(\theta)$ and $r_i^\alpha(\theta)$ are Fresnel transmission and reflection coefficients [19], respectively, for the first and the second cavity mirrors $(i = 1,2)$ correspondent to s- and p-waves $(\alpha = s, p)$, respectively. Both t_i^α and r_i^α are implicitly wavelength-dependent due to wavelength dependence of the complex refractive index of a metal.

3. Discussion

As it is mentioned above the field distribution inside the planar microcavity results from interference of far field beam components focused by the aplanatic lens, which experience multiple reflections inside the cavity. To reinforce comparison to the results of the present modeling in Fig. 1 we reproduce the focal field distribution for RPDB in free space resulting from (4) and (2). As expected [18], the field distribution in the focus is a superposition of in-plane and longitudinal field components, which form a characteristic doughnut (ring) pattern and a narrow spot, respectively. Assuming focusing by a high numerical aperture (NA=1.25) immersion oil objective the maximum intensity of longitudinal components is approximately by a factor of two larger than that of in-plane components. The focal region in longitudinal direction extends approximately to ±λ/2 for both components, which is much larger than the boundaries for the λ/2-cavity approximately shown in Fig. 1(c) and (d) as white dashed lines.
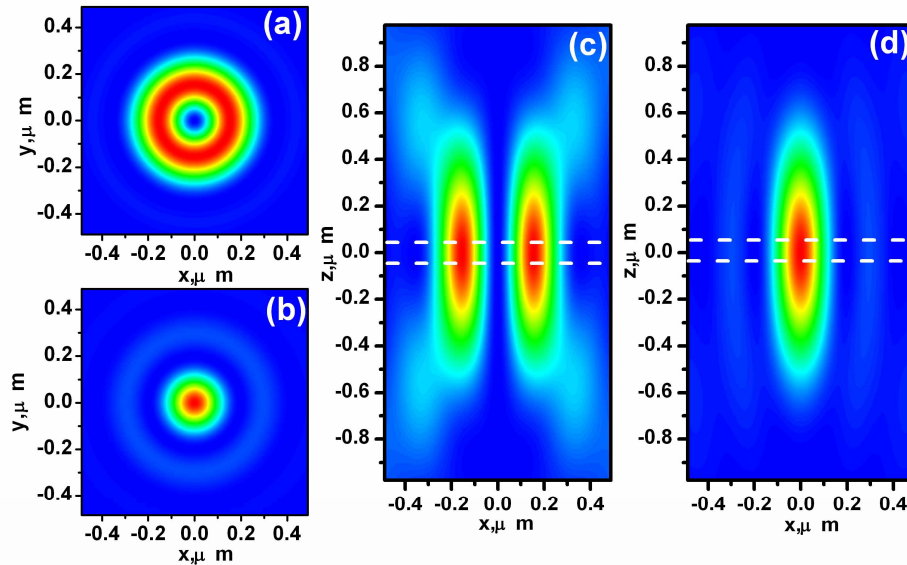
Fig. 1. Field intensity distribution in the focus of RPDB in a homogeneous medium (n_r = 1.518); (a) , (c) cross-section of in-plane field components in x-y and x-z planes, respectively; (b) , (d) cross-sections for longitudinal fields components in x-y and x-z plane, respectively. To reinforce the comparison to following Figures 3 and 4 the boundaries for a 120 nm cavity are shown in (c) and (d) as white dash lines.

In order to illustrate the cavity effect on the field in Fig. 2 we plot f_{xy}^p and f_z^p computed on the basis of (9) and (10), respectively, which are characteristic for the intra-cavity distribution of the longitudinal and in-plane components of the p-polarized plane wave impinging on the cavity at $\theta = 0$. The interference inside the microcavity gives rise to the sharp maximum of the in-plane (x, y) components in the center of the cavity, whereas the longitudinal (z) components of the cavity field are concentrated close to the cavity boundaries.

In view of these observations it is easy to interpret the field intensity distributions for RPDB and APDB focused inside the cavity, which are calculated using (4)-(10) and plotted in Fig. 3. In-plane components of RPDB and APDB have their maximum in the center of the cavity and diminish to zero at the cavity boundaries. The distributions are rotationally symmetric and can be visualized as torroids. In contrast, the longitudinal component of RPDB has a maximum at the cavity boundaries and a minimum in the center. The distribution is also rotationally symmetric and has sand-clock shape. Even for a symmetrical microcavity, the field distributions are not exactly symmetrical with respect to the microcavity center and slightly shifted towards the first mirror. This is an effect of the interference between the rays coming to the focus at different angles and experiencing different diffraction in the microcavity. Another manifestation of this effect is that the diameter of the focal spot for in-plane components becomes by about 20% larger than that in free space.
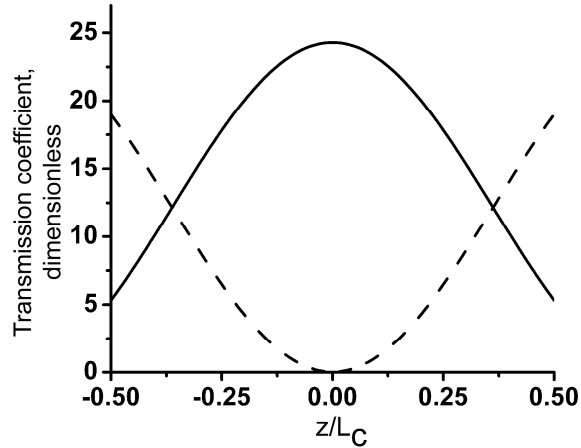
Fig. 2. Intra-cavity transmission coefficient of the $\lambda/2$-microcavity for in-plane (solid line) and longitudinal (dash line) field components according to (9) and (10), respectively, versus longitudinal (z) coordinate, normalized to the cavity thickness (LC). In-plane components have their maximum in the center of the cavity whereas longitudinal components are concentrated at the cavity boundaries.

The notable observation at this point is that focused in-plane components of RPDB exhibit stronger confinement than those for APDB, which results in the maximum intensity for RPDB being four times larger than that of APDB. This effect is due to the difference in the Fresnel reflection coefficients of the metallic mirrors correspondent to p- and s-polarized waves.
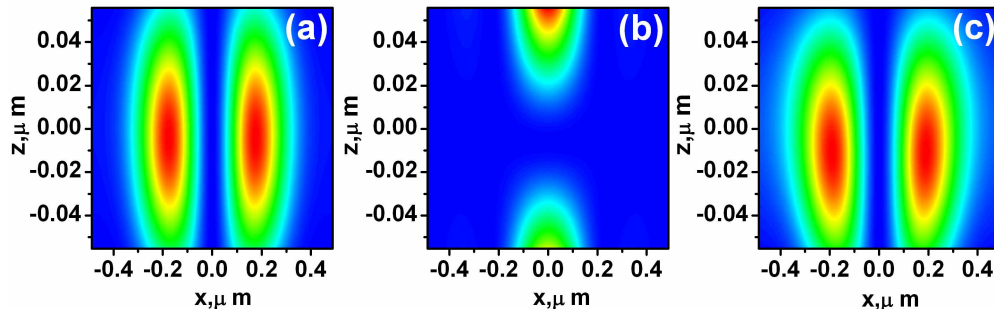

Fig. 3. Field intensity distribution for RPDB and APDB focused inside a 111.5 nm thick Fabri-Perot microcavity satisfying the $\lambda/2$-condition at a wavelength of 488 nm. The beam propagation is from bottom to top; (a) , (b) RPDB in-plane and longitudinal field components, respectively, cross-section in x-z plane; (c) APDB in-plane field components, cross-section in x-z plane. The distributions are rotationally symmetric with respect to the propagation direction (z axis). Parameters for computation: n_{ic}=1.518, L_c =111.5 nm, λ = 488 nm, objective NA = 1.25, thickness of metallic (silver) mirrors 50 nm.

In contrast to APDB and RPDB which are purely s- and p- polarized waves, respectively, the fundamental HGB possesses both of these polarizations. This results in breaking off the rotational symmetry for longitudinal and in-plane field components in the focal spot of a tightly focused x-polarized Gaussian beam [18]. As in the case of doughnut beams our computations according to (1) and (6)-(10) show (cf. Fig. 4) that the maximum of the dominant in-plane E_x component is situated in the center of the cavity, whereas the longitudinal (E_z) components are dominating at the boundaries. Comparison of the focal field intensity distribution in the cavity (cf. Fig. 4) to those in free space [18] shows that the

focal spot is by approximately 20% larger in the cavity than in free space. Due to differences in Fresnel coefficients for s- and p-polarizations and their angular dispersion, the focal spot in the cavity becomes elliptical with longer axis directed perpendicular to the beam polarization direction. Notably, an opposite effect is observed [18] while focusing of HGB on the interface of two dielectrics. There the focal spot is elongated along the polarization direction as a result of strong contribution from longitudinal components that are in the present case suppressed in the microcavity.
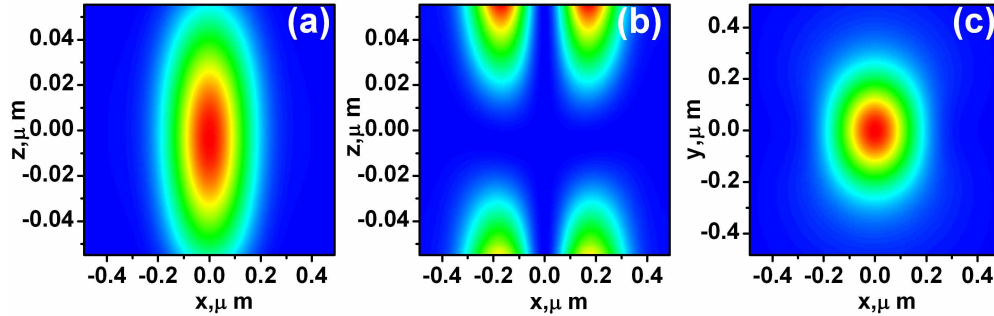

Fig. 4. Field intensity distribution for x-polarized fundamental Hermit Gaussian Beam focused inside a 111.5 nm thick Fabri-Perot microcavity satisfying the $\lambda/2$-condition at a wavelength of 488 nm; (a), (b) intensity of the dominant E_x (in-plane) and E_z (longitudinal) field components, respectively, cross-section in x-z plane; (c) total intensity in the focal spot, cross-section in x-y plane through the center of the cavity. The parameters for the calculation are given in Fig. 3 caption.

To date, many of recent single molecular fluorescence experiments [7] in planar micro-cavities are performed using dyes with considerable Stokes shifts, which imply that the $\lambda/2$-condition for the cavity is fulfilled for the emission wavelength that is longer than the excitation wavelength. In order to account for this situation in Fig. 5. we plot the x-z cross-sections of RPDB and APDB intensity distributions in the microcavity satisfying the $\lambda/2$-condition for 600 nm emission, assuming an excitation beam wavelength of 488 nm. As it can be seen comparing Fig. 3 to Fig. 5, focusing the RPDB in a cavity with a thickness larger than prescribed by the $\lambda/2$-condition for the excitation wavelength results in a tighter focal spot. In particular, the focal spot diameter calculated for the present choice of the parameters equals to the focal spot diameter in free space. Besides, in the distribution of in-plane components noticeable side lobes (i.e. outer rings) appear, the first of them having intensity about 20% of the central doughnut.
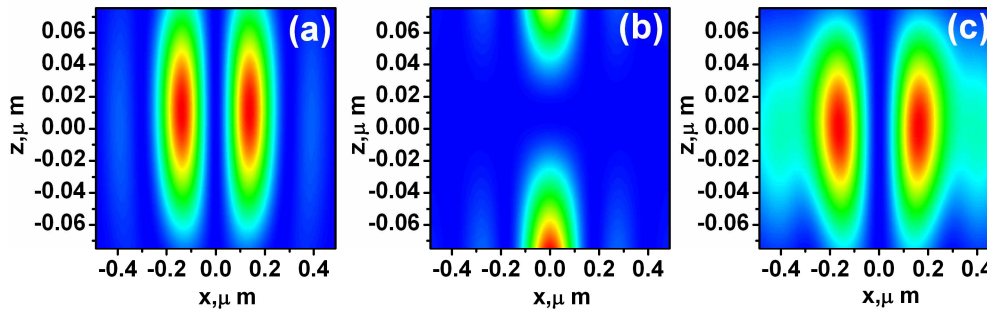

Fig. 5. Field intensity distribution for RPDB and APDB focused inside a 150 nm thick Fabri-Perot microcavity corresponding to a $\lambda/2$-condition for 600 nm wavelength, i.e. larger than in Fig. 3. Cross-sections along x-z plane for RPDB in-plane (a), longitudinal (b), and APDB (c) field components. The parameters for the calculation are given in Fig. 3 caption.

In conclusion we note that the distribution depicted in Fig. 5 quite closely resembles the field distribution in asymmetric cavities, such as the 30 nm / 60 nm cavity investigated in [7],[8], which is due to just minor variation of the phase shift on the mirrors thicker than 30 nm.

4. Excitation patterns of fluorescent beads inside the sub-wavelength microcavity

4.1. Background

In order to experimentally verify the results of the present modeling we use a confocal microscope equipped with APDB and RPDB excitation to monitor raster scanning images for the fluorescent beads incorporated into a sub-wavelength microcavity.

The fluorescent beads consist of a few hundred randomly oriented dye molecules incorporated in a polymer sphere. They are acting as a nano-scale isotropic absorbers and emitters and as convenient probes for monitoring the local field distribution [20]. For such an emitter the raster scanning image acquired by a confocal microscope is given by a convolution of the emitter shape with the microscope point spread function (PSF) that is in turn a product of the excitation PSF and the detection PSF [18]. The isotropic emitter detection PSF can be well approximated by a flat-top shape [21] with the flat-top radius equal to the radius of the confocal pinhole image in the object plane, which for our setup yields about 750 nm. The excitation PSF is given by the excitation field intensity distribution averaged with respect to the random orientation distribution of dye molecules inside the bead. The averaging results in a 50% lower excitation efficiency for in-plane components as compared to excitation efficiency of the longitudinal component, which implies that the excitation PSF $\left(I_{PSF}\right)$ equals to:

$$I_{PSF} = I_z + 0.5 I_\rho ,\tag{11}$$

where I_z and I_ρ are the intensities of the longitudinal and in-plane components, respectively. Since for 488 nm excitation the focal field calculated in the section I of this paper is confined into a 400 nm spot, it is approximately two times narrower than the detection PSF for our setup and eventually determines the resulting microscope PSF. Clearly, for a sufficiently small bead diameter the image acquired with raster scanning confocal microscope is essentially an excitation pattern reproducing the spatial distribution of the excitation field.
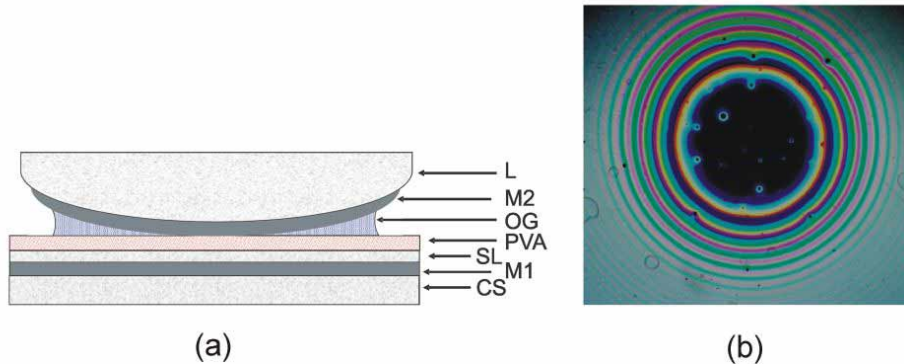

Fig. 6. (a) Microcavity sample. (CS) - Microscope cover slip, (M1) - Bottom Ag mirror (40 nm), (SL) - 30 nm silica spacer layer, (PVA) - PVA layer doped with 20 nm fluorescent beads, (OG) - Optical glue, (M2) - Upper Ag mirror 60 nm, (L) - Lens ; (b) White light transmission pattern of the cavity sample taken with a wide field microscope (magnification 5 times). The inner transmission ring that is used to monitor excitation patterns of the fluorescence beads corresponds to the cavity thickness satisfying the λ/2-condition in the visible spectra range.

4.2. Sample preparation and experimental setup

For the experiment we prepared and characterized a sub-wavelength planar metallic cavity (cf. Fig. 6(a)) according to the method that was similar to the one recently described in [7],[8]. In a nutshell, a thin layer of PVA (about 50 nm) weakly doped (10-9mole/l) with 20 nm nile red fluorescence spheres (Invitrogen) was spin-coated on top of the first cavity mirror that was formed by a 40 nm Ag layer and a 30 nm silica spacer layer thermally evaporated on a microscope cover slip. The second 60 nm Ag mirror was thermally evaporated on a silica plano-convex lens (Thorlabs, diameter 25.4mm, f = 150.0mm). After bringing the lens into a mechanical contact with the cover slip and fixing it with UV cured optical glue (NOA-61, Norland Adhesive) we obtained [8] a sub-wavelength cavity composed of the top (lens) and bottom (cover slip) mirrors.

The experiments were performed with a home made inverted confocal microscope equipped with a high numerical aperture objective (Zeiss, CP Oil Achromat 100x NA=1.25, pupil 4mm) and a 150 μm diameter single photon counting avalanche photo diode (Perkin Elmer, SPCM-AQR-14) serving as a detector unit and confocal pinhole. The white light transmission spectra for microcavity characterization where acquired with a grating spectrograph (Jobin-Yvon, HR-320) in combination with a liquid-nitrogen-cooled CCD camera (LNC/CD-512-TKB1, Princeton Instruments). The experimental set-up and the beam conversion optics used to generate APDB and RPDB for excitation at λ_{exp} =488 nm were exactly as described in a recent group publication [22].

4.3. Experimental results and discussion

Due to the small lens curvature the spacing between the mirrors slowly increases from the (central) contact point to the periphery of the sample making distinct cavity thicknesses accessible by addressing various lateral positions of the sample. At the same time, just sub-nanometer thickness variation resulting from the lens curvature inside the typical scanning area of 2μm by 2μm ensures that the cavity remains locally planar in each addressed point. The white light transmission spectra pattern of the cavity sample depicted in Fig. 6(b) consists of concentric transmission rings corresponding to the cavity resonances in the visible range. By monitoring the maximum of a white light transmission spectrum in the different points of the sample and using the resonance condition for the Fabry-Perot cavity we are able to assign cavity thickness in these points [8]. In the experiment we address the beads located in the first transmission ring of the cavity where the cavity thickness satisfies the λ/2-condition in the visible spectra range, which implies that the intra-cavity optical path including the phase shift on the mirrors equals to one wavelength. The calculated cavity thickness in the first transmission ring can be approximated [8] with an accuracy of few percent by an empirical formula $L = \lambda_{\text{max}} / (2 n_{ic}) - 50$ nm.

In Fig. 7(a) - (e) and (m) - (q) we present excitation patterns obtained using RPDB and APDB, respectively, for five characteristic beads located at different positions inside the first transmission ring of the sample. By virtue of the sample preparation method the beads are confined in a thin PVA layer at approximately constant distance from the bottom cavity mirror. Due to inclination of the top mirror the beads that are located in the green (thinner) side of the first transmission ring are closer to the axial center of the cavity than those located in the red (thicker) side of the ring. Therefore the excitation patterns measured for different cavity thicknesses also correspond to the excitation PSF cross-sections at different relative axial positions inside the λ/2-microcavity.

The measured excitation patterns can be compared to the calculated cross-sections of the RPDB and APDB excitation PSF which are plotted in Fig. 7(g) - (k) and (s) - (w), respectively. The cross-sections are calculated in plane of the cavity according to (4)-(11) at a

constant distance of 60 nm from the bottom cavity mirror. The ratio between this distance and the cavity thickness, which is given in the figures for each of the calculated patterns, ranges from 0.48 to 0.34 that corresponds to a gradual shift from the cavity center between 2% and 16% for the beads selected in the green and red regions, respectively.

In order to highlight the cavity effects and assert the quality of doughnut beams used in the experiment in Fig. 7(f) and (r) we also plot excitation patterns for a bead in free space obtained using APDB and RPDB, respectively. The calculated free space field cross-sections are plotted for RPDB and APDB in Fig. 7(l) and (x), respectively. In all cases we clearly observe very good correspondence between measured and calculated patterns.
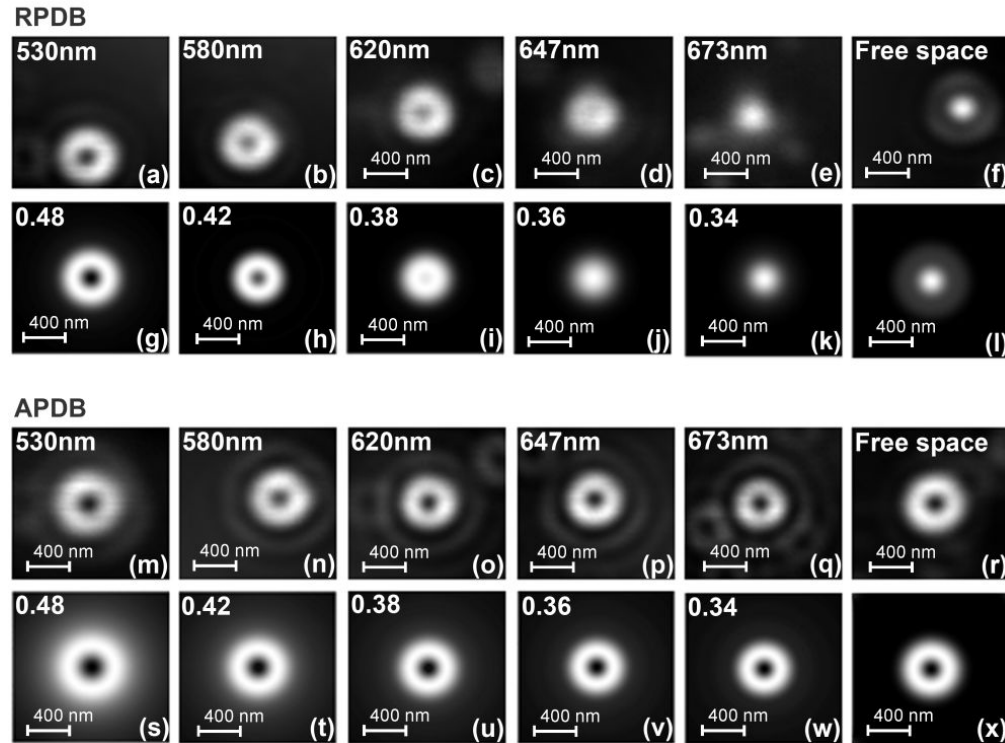

Fig. 7. Raster scanning confocal excitation patterns for the fluorescent beads in the λ/2 - cavity obtained using RPDB (a) - (e) and APDB (m) - (q) excitation. These patterns are measured at five different cavity thicknesses resonant with distinct wavelength (given in the figures) from the bead emission spectra. The Excitation PSF for RPDB (g) - (k) and APDB (s) - (w) calculated for the cavity thicknesses correspondent to respective experimental patterns assuming a constant 60 nm shift from the bottom cavity mirror. The resulting relative shift from the bottom mirror for each of the calculated patterns is given in the figures. Free space excitation patterns for the beads obtained using RPDB (f) and APDB (r) excitation together with the calculated free space excitation PSF for RPDB (l) and APDB (x). Parameters for calculation: objective NA 1.25, excitation wavelength 488 nm, experimentally measured beam waist 1.15 mm.

In essence, the cavity changes the excitation field distribution by suppressing the longitudinal field components in the middle of the cavity and the in-plane field components in vicinity of the mirrors (cf. Figs 3 and 5). This is clearly revealed by experimental and calculated patterns depicted in the Fig. 7 (a-e and g-k). For RPDB excitation the gradual transition from the doughnut excitation pattern resulting from dominating in-plane field components to a spot-like shape correspondent to dominating longitudinal components occurs when the bead is shifted from the microcavity center towards the bottom mirror. In full agreement to the

present modeling the excitation patterns observed for the same beads using APDB have doughnut shape independent on the bead position, since APDB possess only in-plane components.

5. Conclusion

We calculate the electromagnetic field distribution arising in a planar metallic sub-wavelength cavity due to focusing of the fundamental Hermit-Gaussian as well as the azimuthally and radially polarized doughnut beams.

We show that the intra-cavity interference among the focused beam components converging to the focus at different angles results in a strong redistribution of the focal field compared to focusing in free space and causes strong field confinement in the intra-cavity volume. In particular, the in-plane field components have a sharp maximum in the focal point and diminish nearly to zero at the cavity boundaries, whereas longitudinal field components are concentrated at the cavity boundaries and negligible in the middle of the cavity. Intensity distributions for the radially and azimuthally polarized beams retain their free space rotational symmetry along the beam propagation direction, whereas the elliptical focal spot of the Gaussian beam is elongated in perpendicular to the beam polarization direction.

In order to experimentally assert the results of the present modeling we measure the APDB and RPDB excitation patterns for the fluorescence beads incorporated in a $\lambda/2$ metallic microcavity. We observe very good correspondence between calculated and measured excitation patterns that unambiguously verify our model.

Since the excitation field distribution ultimately determines the excitation efficiency of SM emitters inside the cavity the results have a direct implication for the optimal design of sub-wavelength planar micro-resonators for single molecular imaging and spectroscopy aiming on nano-photonics applications.